Phase diagrams of confined square lattice linked polygons

E. J. Janse van Rensburg [1,*] and E. Orlandini[2,†]

[1]*Department of Mathematics and Statistics, York University, Toronto, Ontario M3J 1P3, Canada*

[2]*Dipartimento di Fisica e Astronomia "Galileo Galilei", Universitá degli studi di Padova, 8-35131 Padova, Italia*

(Received 9 September 2021; accepted 10 December 2021; published 23 December 2021)

The phase diagrams of two models of two confined and dense two-dimensional ring polymers are examined numerically. The ring polymers are modeled by square lattice polygons in a square cavity and are placed to be either unlinked or linked in the plane. The phase diagrams of the two models are found to be a function of the placement of the ring polymers and include multicritical points where first-order and continuous phase boundaries meet. We estimate numerically the critical exponents associated with the phase boundaries and the multicritical points.

DOI: 10.1103/PhysRevE.104.064134

I. INTRODUCTION

Entanglement is an important factor determining the physical properties of polymers and biopolymers [1–4]. Knotting and linking of polymers are aspects of their entanglement and have been studied extensively [5–7] in lattice models [3,8–10], also in confining spaces [11], or when adsorbed [12], or when the polymer is beyond the θ transition in the collapsed or dense phase [13,14]. It is now known that knotting is suppressed in a lattice polygon stretched in one direction, or stretched by a force [15,16], but enhanced when the polygon is compressed in a confining space [11]. It is also known that other thermodynamic quantities, such as pressure, is a function of knotting [17], while recent studies of compressed lattice knots show that osmotic pressure for finite length polymers is a function of knotting [18] (see Ref. [19] for results for linear compressed lattice polymers).

In this paper we determine the phase diagrams of a model of a pair of dense ring polymers in the plane and confined to a cavity (a convex region). The model consists of two square lattice polygons placed inside a confining square in two topologically distinct ways. The splittable placement is called the *unlinked* case, and the unsplittable placement the *linked* case (see Fig. 1). In the square lattice the polygons are compressed by the confining square and so are models of dense ring polymers in two dimensions [20] (for example, ring polymers adsorbed on a surface and freely fluctuating within a cavity). We are primarily interested in the phase diagrams of these topologically distinct placements as a function of the chemical potentials of the monomers in the polymers. Our numerical data show that the phase diagrams are dependent on the topology of the two placements, as noted for cubic lattice models of knotted and linked lattice polygons above. The two-dimensional placements of the polygons also model two ring polymers squeezed in a very narrow slab between a piston and a (repulsive) surface; see, for instance, Refs. [21,22]. In three dimensions these models would, for example, describe two vesicles (random surfaces homeomorphic to 2-spheres) placed in two distinct ways and compressed in a cavity.

If the two polygons in Fig. 1 are labeled by 1 and 2, such that the outer polygon in the linked case carries label 1, then the partition functions of the two models are given by

$$\mathcal{U}_L(\alpha,\beta) = \sum_{n1,n2} u_L(n_1,n_2)\, e^{\alpha n_1}\, e^{\beta n_2}, \tag{1}$$

$$\mathcal{L}_L(\alpha,\beta) = \sum_{n1,n2} \ell_L(n_1,n_2)\, e^{\alpha n_1}\, e^{\beta n_2}. \tag{2}$$

Here, n_1 and n_2 are the lengths of polygons 1 and 2, respectively, while the number of conformations (states) of two unlinked and linked polygons in a confining square of side-length L and area L^2 lattice sites are denoted by $u_L(n_1,n_2)$ and $\ell_L(n_1,n_2)$, respectively. The parameters (α,β) are related to the chemical potentials of the monomers (vertices) along the polygons. If $\alpha \ll 0$ and $\beta \ll 0$, then short polygons dominate the partition functions. This corresponds to a phase of short polygons exploring the area of the confining square, and we call this the *empty phase*. If either $\alpha \gg 0$ or $\beta \gg 0$, or both, then the partition functions are dominated by one or two long polygons filling the square, and the model is in a *dense phase*.

If one considers our models as $L \times L$ systems with sites either occupied or vacant subject to topological constraints (so that the occupied sites form a pair of lattice polygons), then the (canonical) free energies of the two models are defined by

$$f_L(\alpha,\beta) = \frac{1}{L^2}\log \mathcal{U}_L(\alpha,\beta), \quad \text{and} \tag{3}$$

$$g_L(\alpha,\beta) = \frac{1}{L^2}\log \mathcal{L}_L(\alpha,\beta). \tag{4}$$

If the parameters (α,β) are considered to be chemical potentials of vertices along the polygons, then f_L and g_L are the corresponding grand potentials of the models, and their first- and second-order derivatives are the concentrations and

*rensburg@yorku.ca

†orlandini@pd.infn.it

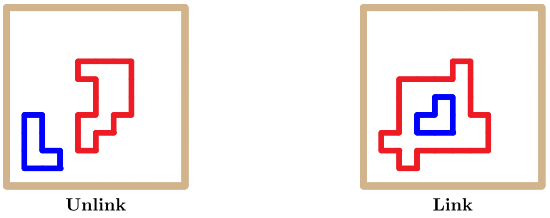

FIG. 1. Lattice models of the unlinked and linked pairs of lattice polygons in a confining square of side-length L.

variances of the concentrations, respectively. In this paper we shall refer to f_L and g_L as *free energies*, but to their derivatives as *mean concentrations* and *variances* (of the mean concentrations). Notice that f_L and g_L are analytic functions of (α, β), and so phase boundaries will only exist in the $L \to \infty$ limit. In small finite systems, finite-size effects may be important, and phase boundaries are normally seen as peaks in the variances of concentrations, or as sharp changes in the concentrations. In this paper we are able to choose L large enough that in some cases free energies can be fitted to (nonanalytic) absolute value functions, concentrations are approximately step functions, and the variances of concentrations have sharp spikes when crossing phase boundaries.

Our finite-size data show that the phase diagrams of these models each include a multicritical point where three phase boundaries meet. In the unlinked model the multicritical point is the nexus of two continuous and one first-order phase boundary, while in the linked model, it is the meeting point of one continuous and two first-order phase boundaries, as shown in Fig. 2. The locations of the multicritical points are obtained by examining the polygon generating function $P(t)$

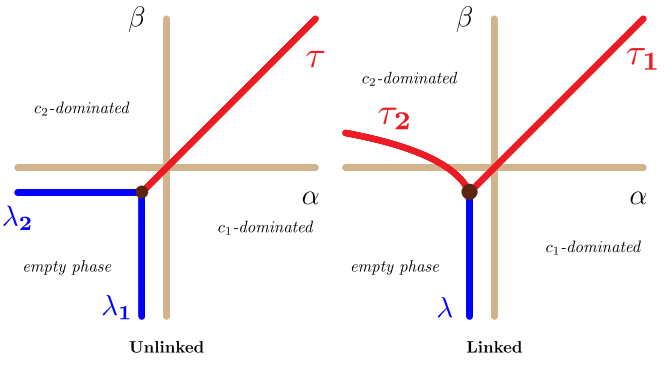

FIG. 2. The phase diagrams of the unlinked (left) and linked (right) models as determined in this paper. In the unlinked model the multicritical point is located at (α_c, α_c), where $\alpha_c = -\log \mu_2$ in the $L \to \infty$ limit (and μ_2 is the growth constant of square lattice polygons [23–25]). The location (α_c, β_c) of the multicritical point in the linked model is more difficult to determine, where again $\alpha = -\log \mu_2$ in limit as $L \to \infty$. The phase boundaries (λ_1, λ_2) in the unlinked model, and λ in the linked model, are continuous transitions, while the τ phase boundaries in both models are first-order phase transitions. These phase boundaries separate empty phases from dense phase, namely, a c_1-dominated phase when the first polygon (or the outer polygon in the linked model) is dense in the confining square, or a c_2-dominated phase when the second (or the inner polygon in the linked model) is dense in the confining square.

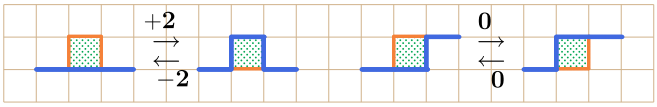

FIG. 3. The BFACF elementary moves in the square lattice [26,27]. On the left is the positive move (left to right), and the negative move (right to left). On the right is the neutral move.

given by

$$P(t) = \sum_{n=0}^{\infty} p_n t^n, \tag{5}$$

where p_n is the number of square lattice polygons of length n. The radius of convergence of $P(t)$ is $t_c = 1/\mu_2$ [23–25] (where μ_2 is the growth constant of square lattice self-avoiding walks), so that if $L = \infty$, then the two polygons contributing to the partition function in Eq. (1) become independent and the locations of the critical lines λ_1 and λ_2 are along vertical and horizontal lines with $\alpha_c = \beta_c = -\log \mu_2$. Similarly, the location of the critical line λ in the linked model is along the vertical line with $\alpha_c = -\log \mu_2$ since for $\beta < -\log \mu_2$ the inner polygon is short and the outer polygon can expand when $\alpha > -\log \mu_2$.

In this paper our aim is to examine the phase diagrams in Fig. 2 numerically by simulating a 20×20 system using Monte Carlo methods. Our data show that this finite size system is large enough to enable us to determine the phase diagram of the system with good accuracy, and to obtain reasonable estimates of the critical exponents associated with each phase boundary.

Sampling self-avoiding walks or polygons in a dense phase is a notoriously difficult numerical problem [28] but for the unlinked model a parallel implementation [29] of the GAS algorithm [30] proved effective. In the linked model we instead used the GARM [31] algorithm after the GAS algorithm failed to converge. These algorithms were implemented with BFACF elementary moves [26,27] (see Fig. 3) to approximately enumerate states in the models giving estimates of $u_L(n_1, n_2)$ and $\ell_L(n_1, n_2)$ in Eqs. (1) and (2). Note that both algorithms are in a class of approximate enumeration algorithms derived from the Rosenbluth algorithm [32] and they directly estimate $u_L(n_1, n_2)$ and $\ell_L(n_1, n_2)$ in Eqs. (1) and (2). The GAS and GARM algorithms are designed to sample from "flat distributions" over the state space of the models. For more details, see Refs. [30,31], and also in particular the PERM and flatPERM algorithms [33,34] on which these are based. Convergence in the linked model was improved dramatically by including the neutral (total length preserving) move shown in Fig. 4, in addition to the standard BFACF elementary moves. Additionally, we used a multiple Markov Chain [28] implementation of the BFACF algorithm [26,27] to sample metric and other properties of the polygons across phase boundaries to further examine the nature of the transitions shown in Fig. 2. We note that an alternative approach to our numerical methods would be to enumerate pairs of polygons directly in a confining square in the square lattice. Such exact enumeration methods for self-avoiding walks and polygons in confining squares are described and presented in

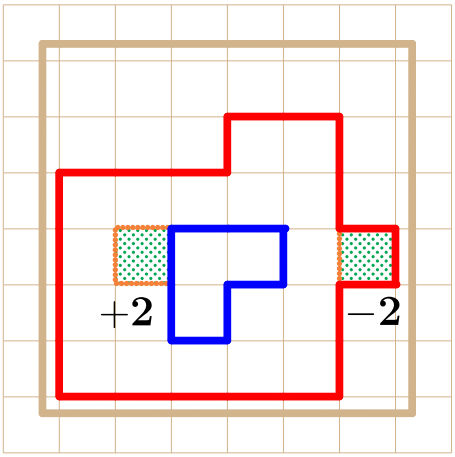

FIG. 4. A neutral move on the pair of polygons in the linked model consisting of a positive (+2) move on the inner polygon and a negative (−2) move on the outer polygon. The overall length of the two polygons remains unchanged, but they exchange edges to increase and decrease their lengths, respectively.

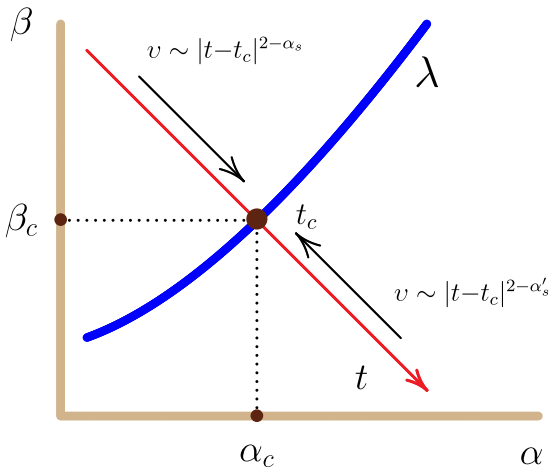

FIG. 5. A schematic drawing of the transverse scaling axis crossing a phase boundary when $t = t_c$ in the phase diagram of the unlinked or linked models. The free energy $\upsilon(\alpha, \beta)$ is singular when $t = t_c$. If the transition is continuous, then there are critical exponents (α_s, α'_s) such that $\upsilon(\alpha, \beta) \sim |t-t_c|^{2-\alpha_s}$ as $t \to t_c^-$ and $\upsilon(\alpha, \beta) \sim |t-t_c|^{2-\alpha'_s}$ as $t \to t_c^+$.

Refs. [35,36] and will be effective for giving exact partition functions in Eqs. (1) and (2). While our approach only gives approximate estimates, our data will show that these estimates are precise enough to determine accurately the phase diagrams of the models.

In the next section we review the critical behavior in the phase diagrams in Fig. 2, before we discuss our numerical results, and examine the behavior of several observables in these models.

II. CRITICALITY IN MODELS OF UNLINKED AND LINKED DENSE POLYGONS

It is not known that the thermodynamic limits (in the $L \to \infty$ limit) exist in our models (the methods of Refs. [37] and [38] can be used to show that some models, similar to those in Fig. 1, have thermodynamic limits). Assuming existence of the thermodynamic limits, define

$$\upsilon(\alpha, \beta) = \lim_{L\to\infty} f_L(\alpha, \beta), \quad \text{and} \tag{6}$$

$$\omega(\alpha, \beta) = \lim_{L\to\infty} g_L(\alpha, \beta). \tag{7}$$

These are the limiting free energies of the models, and we use the theory in Ref. [39] to determine the nature of the transitions along the critical lines in Fig. 2.

Along an axis in the phase diagram, parametrized by t and crossing a critical curve at $t = t_c$ (see Fig. 5), the singular part of $\upsilon(\alpha, \beta)$, denoted by $\upsilon_s(\alpha, \beta)$, is expected to exhibit powerlaw behavior given by

$$\upsilon_s(\alpha, \beta) \sim \begin{cases} |t - t_c|^{2-\alpha_s}, & \text{if} \quad t \to t_c^-, \\ |t - t_c|^{2-\alpha'_s}, & \text{if} \quad t \to t_c^+, \end{cases} \tag{8}$$

where α_s and α'_s are critical exponents characteristic of the transition. Similar expressions hold for the limiting free energy $\omega(\alpha, \beta)$ of the linked model.

The functions $\upsilon(\alpha, \beta)$ and $\omega(\alpha, \beta)$ are approximated by $f_L(\alpha, \beta)$ and $g_L(\alpha, \beta)$ in Eq. (3) when L is finite. In this case there are finite-size corrections to scaling which modify Eq. (5) by introducing a *finite-size* crossover exponent ϕ_s. For large L the finite-size corrections are small and are confined to a region close to the critical point. In this case it may be possible to extract critical exponents directly from numerical data.

The phase diagrams in Fig. 2 include multicritical points where curves of first-order and continuous transitions meet. This is shown schematically in Fig. 6, where a curve of first-order transitions (τ) meets a curve of continuous transitions (λ) at the *tricritical point* (α_c, β_c). Approaching the tricritical point along the τ phase boundary, the singular part of $\upsilon(\alpha, \beta)$ scales as

$$\upsilon_s(\alpha, \beta) \sim |t - t_c|^{2-\alpha_u}, \tag{9}$$

where t is the coordinate of a scaling axis along τ. Transverse to the λ phase boundary at the multicritical point,

$$\upsilon_s(\alpha, \beta) \sim |s - s_c|^{2-\alpha_t}, \tag{10}$$

where s is the coordinate of the transverse scaling axis. Since $\upsilon(\alpha, \beta)$ is a function of two variables, consistency of these scaling laws requires that there exists a *crossover exponent* ϕ and scaling function F such that $F(x) \sim x^{2-\alpha_u}$ and

$$\begin{aligned} \upsilon_s(\alpha, \beta) &\sim |s - s_c|^{2-\alpha_t} F(|s - s_c|^{-\phi} |t - t_c|) \\ &= |t - t_c|^{2-\alpha_u} (|s - s_c|^{-(2-\alpha_t)/(2-\alpha_u)} |t - t_c|)^{\alpha_u - 2} \\ &\quad \times F(|s - s_c|^{-\phi} |t - t_c|) \\ &= |t - t_c|^{2-\alpha_u} F_1(|s - s_c|^{-\phi} |t - t_c|), \end{aligned} \tag{11}$$

where $F(x) = x^{2-\alpha_u} F_1(x)$ and provided that the crossover exponent is given by

$$\phi = \frac{2 - \alpha_t}{2 - \alpha_u}. \tag{12}$$

Similar expressions hold for $w(\alpha, \beta)$ of the linked model, with its exponents α_u, α_t, and crossover exponent ϕ.

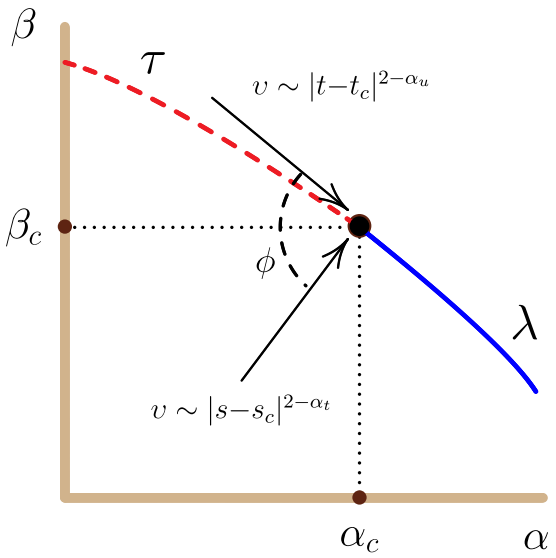

FIG. 6. A tricritical point where a critical curve of first-order transitions (τ) meets a line of continuous transitions (λ). Approaching the tricritical point along τ the free energy scales as $\upsilon(\alpha,\beta) \sim |t-t_c|^{2-\alpha_u}$, where t is a coordinate along τ. Along a second axis through the tricritical point and transverse to λ, the free energy scales as $\upsilon(\alpha,\beta) \sim |s-s_c|^{2-\alpha_t}$, where s is a coordinate transverse to λ. The scaling of $\upsilon(\alpha,\beta)$ close to the tricritical point is consistent provided that their exists a crossover exponent ϕ relating to the exponents α_u and α_t by $\phi = (2-\alpha_t)/(2-\alpha_u)$.

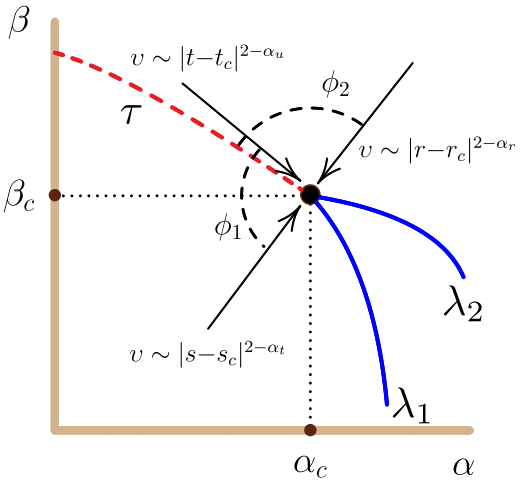

FIG. 7. A multicritical point where a critical curve of first-order transitions (τ) meets two curves of continuous transitions (λ_1 and λ_2). Approaching the multicritical point along τ the free energy scales as $\upsilon(\alpha,\beta) \sim |t-t_c|^{2-\alpha_u}$, where t is a coordinate along τ. Along a second axis through the multicritical point and transverse to λ_1, the free energy scales as $\upsilon(\alpha,\beta) \sim |s-s_c|^{2-\alpha_t}$, where s is a coordinate transverse to λ_1. The scaling of $\upsilon(\alpha,\beta)$ between τ and λ_1 close to the multicritical point is consistent provided that there exists a crossover exponent ϕ_1 relating the exponents α_u and α_t by $\phi_1 = (2-\alpha_t)/(2-\alpha_u)$. Similarly, transverse to λ_2 the free energy scales as $\upsilon(\alpha,\beta) \sim |r-r_c|^{2-\alpha_t}$, where r is a coordinate transverse to λ_2. This defines a crossover exponent ϕ_2 relating the exponents α_u and α_r by $\phi_2 = (2-\alpha_r)/(2-\alpha_u)$.

In our models the phase diagrams of both the unlinked and linked models will be shown to include a multicritical point, generalizing tricritical scaling as shown in Fig. 6 by the introduction of additional crossover exponents relating scaling along first-order and continuous phase boundaries. In Fig. 7 we show the case where two continuous phase boundaries λ_1 and λ_2 meet a curve of first-order phase transitions τ in a multicritical point. In this case there is crossover behavior on either side of the τ phase boundary towards the λ_1 and λ_2 phase boundaries. On each side crossover exponents ϕ_1 and ϕ_2 control crossover scaling. We shall show that the phase boundary of the unlinked model has the geometry shown in Fig. 7, albeit symmetric so that $\phi_1 = \phi_2$ (as shown in Fig. 2). The phase diagram of the linked model, in contrast, has a multicritical point where two curves τ_1 and τ_2 of first-order phase transitions meet a curve λ of continuous transitions. In this model the situation is similar to that shown in Fig. 7, but now with scaling along parallel axes on each of the τ_1 and τ_2 phase boundaries, and transverse to the λ phase boundary. This gives crossover scaling between τ_1 and λ with crossover exponent ϕ_1, and similarly between τ_2 and λ with crossover exponent ϕ_2.

III. NUMERICAL RESULTS

Simulations on the unlinked model with $L = 20$ were performed using the GAS algorithm [30] with BFACF elementary moves [26,27] (Fig. 3). A parallel implementation (similar to the implementation of PERM in Ref. [29]) using 8 threads and shared data structures was run for 2000 started sequences (or *tours*) each of length 10^7 iterations. This amounts to a total of 1.6×10^{11} sampled configurations (iterations). The simulation converged in reasonable time to very stable estimates of $u_L(n_1, n_2)$ [see Eq. (1)]. The linked model proved far more difficult and did not converge successfully, notably because the GAS algorithm failed to effectively sample states with $n_1 < n_2$ (that is, a short outer polygon with enclosed area filled with a long inner polygon as expected in the c_2-dominated phase). Using the GARM algorithm instead, implemented with BFACF elementary moves and an additional neutral move (see Fig. 4), proved effective, and a parallel implementation with 12 parallel threads, sampling along GARM sequences for a total of $12 \times 4.03 \times 10^5$ tours, converged in reasonable time (see Ref. [29]).

The GAS and GARM algorithms are approximate enumeration algorithms producing estimates of the microcanonical partitions $u_L(n_1, n_2)$ and $\ell_L(n_1, n_2)$ in Eqs. (1) and (2). This gives estimates of the free energies f_L and g_L [Eqs. (3) and (4)] and in the event that L is large enough, we obtain accurate approximations to the limiting free energies $\nu(\alpha,\beta)$ and $\omega(\alpha,\beta)$ in Eqs. (6) and (7). Our simulations show that $L = 20$ is sufficiently large, and that it will be challenging to perform simulations for $L > 20$, in particular for the linked model.

A. The phase diagram of two unlinked confined square lattice polygons

In Fig. 8(a) a density plot of $f_L(\alpha,\beta)$ for $L = 20$ is shown, with the left bottom color low, and the right and top colors high. The free energy shows clear signs of transitions, and this is also confirmed by plotting other observables related

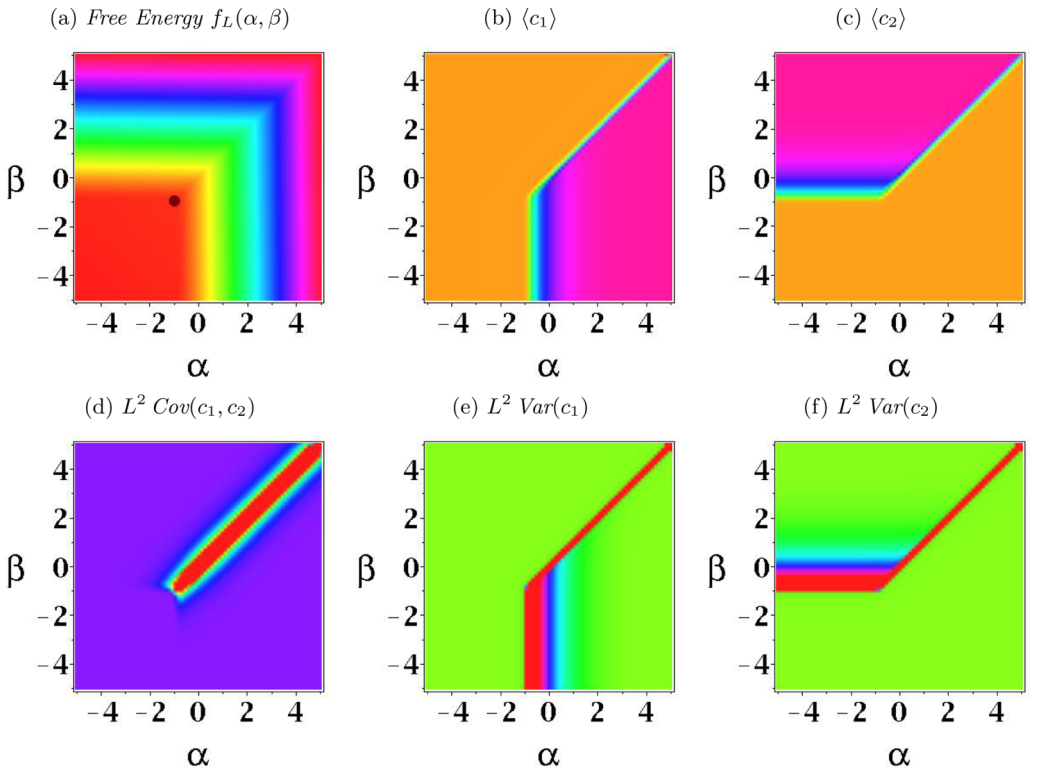

FIG. 8. The free energy $f_L(\alpha,\beta)$ of the unlinked model for $L = 20$ (top left), and its first and second derivatives. Proceeding clockwise from the top middle, the energies $\langle c_1\rangle$ and $\langle c_2\rangle$, the specific heats (variances) $\mathrm{Var}(c_2)$ and $\mathrm{Var}(c_1)$, and the covariance $\mathrm{Cov}(c_1, c_2)$ of c_1 and c_2. The concentrations c_1 and c_2 are negatively correlated, and show sharp transitions along the main diagonal for $\alpha = \beta > \alpha_c$. The location of the multicritical point in the model is denoted by a bullet in panel (a).

to the first and second derivatives of $f_L(\alpha,\beta)$. The mean concentrations of vertices in each polygon are related to the mean lengths of the polygons by

$$\langle c_1\rangle = \langle n_1\rangle/L^2 = \frac{d}{d\alpha} f_L(\alpha,\beta). \tag{13}$$

The concentration of the second polygon is similarly given by $\langle c_2\rangle = \langle n_2\rangle/L^2 = \frac{d}{d\beta} f_L(\alpha,\beta)$. Density plots of $\langle c_1\rangle$ and $\langle c_2\rangle$ are shown in Figs. 8(b) and 8(c). These plots show rapid change in the mean concentrations of one, or both, the polygons when phase boundaries are crossed.

The variance of the concentration c_1 is given by

$$\mathrm{Var}(c_1) = \frac{1}{L^4}\mathrm{Var}(n_1) = \frac{1}{L^2}\frac{\partial^2}{\partial\alpha^2} f_L(\alpha,\beta) \tag{14}$$

and in Fig. 8(e) a density plot of $L^2\,\mathrm{Var}(c_1)$ is shown, and this shows a phase boundary (where $\mathrm{Var}(c_1)$ is large) separating phases where $\langle c_1\rangle$ is small from a phase where $\langle c_1\rangle$ is large. A similar plot of $L^2\,\mathrm{Var}(c_2)$ is shown in Fig. 8(f) for the concentration c_2 of the second polygon. The covariance of c_1 and c_2 is given by

$$\begin{aligned}\mathrm{Cov}(c_1,c_2) &= \frac{1}{L^4}(\langle n_1 n_2\rangle - \langle n_1\rangle\langle n_2\rangle)\\ &= \frac{1}{L^2}\frac{\partial^2}{\partial\alpha\,\partial\beta} f_L(\alpha,\beta),\end{aligned} \tag{15}$$

and $L^2\,\mathrm{Cov}(c_1, c_2)$ is plotted in Fig. 8(d). The covariance is small negative in most of the plot, but spikes to large negative along a phase boundary which runs along the diagonal with points (α,β) where $\alpha = \beta > \alpha_c$ and starting in a multicritical point (α_c,α_c) since the phase diagram is symmetric under exchange $\alpha \leftrightarrow \beta$.

These results numerically confirm the phase diagram of the unlinked model shown in Figs. 2 and 9. The multicritical point (α_c,α_c) is located at the meeting point of three phase boundaries. The phase transition along the main diagonal, denoted by τ, is a line of transitions starting in the multicritical point running into the first quadrant. Up to numerical accuracy, above and to the left of τ the free energy is only a function of β, and to the right and below it, only a function of α. This shows that τ is a first-order phase boundary separating a phase where $\langle c_2\rangle$ is large from a phase where $\langle c_1\rangle$ is large. These are the c_2-*dominated* and c_1-*dominated* phases, respectively.

Two additional phase boundaries are meeting at the multicritical point, namely, a line of transitions λ_1 running vertically into the multicritical point and a line of transitions λ_2 running horizontally into the multicritical point. The vertical phase boundary separates a phase where both $\langle c_1\rangle$ and $\langle c_2\rangle$ are small (this is the *empty phase*) from a c_1-dominated phase. Similarly, the horizontal phase boundary separates the empty phase from a c_2-dominated phase.

Note that, since $f_L(\alpha,\beta)$ is an analytic function of (α,β), these phases and phase boundaries exist only in the $L \to \infty$ limit. In our data the phase boundaries manifest themselves as peaks in the variances or sharp changes in the mean concentrations. The location of the multicritical point is obtained by observing that the radius of convergence of

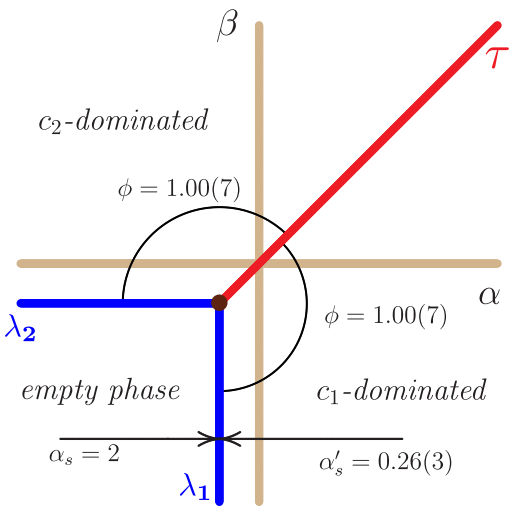

FIG. 9. Crossover exponents between τ and the λ_1 and λ_2 critical curves around the multicritical point in the phase diagrams of the unlinked models. This phase diagram is symmetric over the main diagonal, so that the crossover exponents ϕ on either side have the same value.

the polygon partition function $P(t)$ in Eq. (2) is $t_c = 1/\mu_2$, so that if $L = \infty$, then the two polygons contributing to Eq. (3) become independent and the critical points are determined by the polygon generating function. This gives $\alpha_c = \beta_c = -\log \mu_2 \approx -0.97$.

Critical scaling in the unlinked model

The τ phase boundary: In Fig. 10 the free energy, mean concentrations and variances for $L = 20$ are plotted as a function of α from the point (0,5) along the line segment to (5,0). The critical point (where the τ phase boundary is crossed) corresponds to $\alpha = 2.5$, and this is seen in the plot of the free energy f_L in Fig. 10(a). The phase transition along the τ phase boundary is a first-order transition to numerical accuracy, as the limiting free energy in Eq. (6) is accurately approximated by f_L for $L = 20$, and f_L can be directly modeled by an absolute value function. Indeed, using the five-parameter model

$$\upsilon(\alpha, 5{-}\alpha) = a_0 + a_1\,|\alpha - a_c|^{2-\alpha_s} + a_2\,(\alpha - a_c)^2 \qquad (16)$$

a nonlinear fit (done using the *NonlinearFit* function in Maple [40]) can be performed to obtain estimates of the exponent $2{-}\alpha_s$. Ignoring the quadratic term (by putting $a_2 = 0$) gives the regression

$$\upsilon(\alpha, 5{-}\alpha) \approx 2.810 + 0.975\,|\alpha - 2.498|^{1.003}. \qquad (17)$$

Repeating the fit with a_2 as an additional parameter gives instead

$$\upsilon(\alpha, 5{-}\alpha) \approx 2.810 + 0.976\,|\alpha - 2.499|^{1.006} + 0.00153\,(\alpha - 2.499)^2. \qquad (18)$$

Notice the very small coefficient of the quadratic term, showing that the free energy is very closely approximated by the absolute value term. These fits give the critical point at $a_c = 2.498$ (compared to its exact value 2.5 by symmetry) and the estimate of the exponent $2{-}\alpha_s = 2{-}\alpha'_s \approx 1.003$ [see Eq. (5)]. These results show that, even in this finite-size model, with $L = 20$, the free energy is well approximated by a nonanalytic function, having a sharp transition at the critical point.

As in Fig. 5 one may now estimate the scaling exponent associated with the τ phase boundary. Taking as error bar the difference in the estimates in Eqs. (17) and (18),

$$2 - \alpha_s = 2 - \alpha'_s = 1.003 \pm 0.003. \qquad (19)$$

This is consistent with the transition across the τ phase boundary being first order.

The λ_1 and λ_2 phase boundaries: Next, consider the transition across the λ_1 phase boundary by calculating the free energy along the line segment from $(-5, -2)$ to $(5, -2)$. The results are plotted in Fig. 11 as a function of α. The graphs in Fig. 11(b) of the concentrations $\langle c_1\rangle$ and $\langle c_2\rangle$ show that the transition across the λ_1 phase boundary does not have a step-like increase, unlike the case for the τ phase boundary. Since the λ_1 phase boundary in Fig. 9 is a vertical line and $\alpha_c \approx -0.97$, the transition across λ_1 is expected to occur at α_c, and our data are consistent with this. The critical exponent associated with the transition is defined by Eq. (8), and since

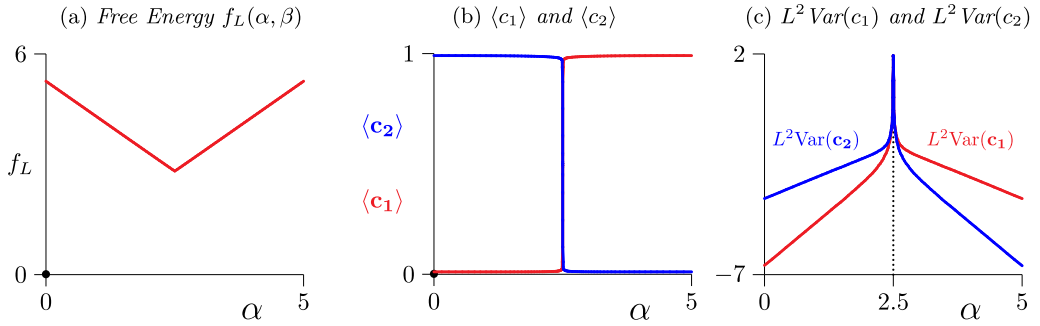

FIG. 10. The free energy, mean concentrations and variances of the unlinked model as a function of α along the line crossing the τ phase boundary between the points (0,5) to (5,0) in the phase diagram in Fig. 9. These data were calculated for $L = 20$, but shows that the free energy is to numerical accuracy an absolute function, nonanalytic on the τ phase boundary. The mean concentrations $\langle c_1\rangle$ and $\langle c_2\rangle$ are approximately step functions at the critical line, while the variances, plotted on a logarithm vertical scale, develop sharp spikes at the critical point, while having very small values (less than 10^{-3}) away from the critical point.

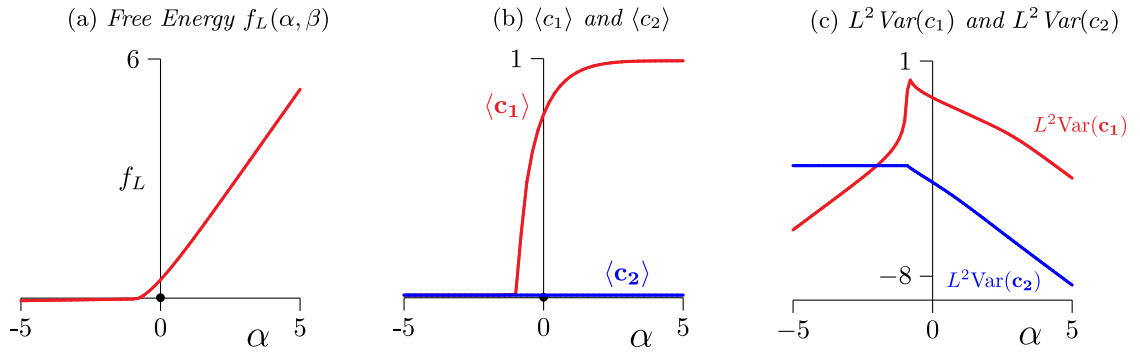

FIG. 11. The free energy, mean concentrations, and variances of the unlinked model as a function of α along the line from the point $(-5,-2)$ to $(5,-2)$ crossing λ_1 in the phase diagram in Fig. 9. The free energy shows a transition at approximately $\alpha_c \approx -\log\mu_2 \approx -0.97$, and this seen in the behavior of the mean concentration $\langle c_1\rangle$. Our analysis strongly suggests that this transition between the empty and the c_1-dominated phase is continuous. Notice that $\langle c_2\rangle$ appears to be unchanged in the middle graph, but if the logarithm of variances are plotted, then $\mathrm{Var}(c_2)$ is singular at the critical point, going from constant into a steady decline. Since our model is symmetric in $\{c_1, c_2\}$, these graphs will be unchanged (except with c_1 and c_2 interchanged) if instead these quantities are calculated along the line segment from $(-2,-5)$ to $(-2,5)$ which crosses over the phase boundary λ_2 separating the empty and the c_2-dominated phases.

the free energy f_L in Fig. 11 is (up to numerical accuracy) a constant for $\alpha < \alpha_c$ we conclude that $2-\alpha_s = 0$ along the λ_1 phase boundary as $\alpha \to \alpha_c^-$.

If $\alpha > \alpha_c$, then the concentration $\langle c_1\rangle$ increases sharply at the critical point [as shown in Fig. 11(b)]. As α increases in size, one expects that the first polygon becomes dense and then fills the confining square, and $\langle c_1\rangle \to 1$. In view of Eq. (8),

$$\langle c_1\rangle \sim |\alpha-\alpha_c|^{1-\alpha_s'}, \text{ for } \alpha \to \alpha_c^+ \text{ and } \beta = -2. \tag{20}$$

The exponent can be estimated by plotting $\log\langle c_1\rangle/\log|\alpha-\alpha_c|$ as a function of $1/\log|\alpha-\alpha_c|$. This is improved if we subtract from $\langle c_1\rangle$ its (small but nonzero) value $\langle c_1\rangle|_{\mathrm{crit}}$ at $\alpha = \alpha_c$, to zero it at the critical point. This removes a background term due to the finite size of our model. Defining

$$\log\langle c_1\rangle_s = \log(\langle c_1\rangle - \langle c_1\rangle|_{\mathrm{crit}}) \tag{21}$$

we get the model

$$\begin{aligned}\gamma &= \log\langle c_1\rangle_s/\log|\alpha-\alpha_c| \\ &= (1-\alpha_s') + C/\log|\alpha-\alpha_c| + \ldots\end{aligned} \tag{22}$$

Choosing $\alpha_c = -0.97$ and then plotting γ as a function of $1/\log|\alpha-\alpha_c|$ for $-0.95 \leqslant \alpha \leqslant 0$ gives the graph in Fig. 12. This graph is almost a straight line, except at points where α approaches α_c. Fitting a linear function in $1/\log|\alpha-\alpha_c|$ to the graph gives the estimate $1-\alpha_s' \approx 0.545$, and fitting a quadratic instead gives $1-\alpha_s' \approx 0.516$. The difference in these two estimates is taken as a confidence interval in the estimate. Taken together,

$$\alpha_s = 2 \quad \text{and} \quad \alpha_s' \approx 0.45 \pm 0.03 \tag{23}$$

along the λ_1 phase boundary.

Thus, the transitions along the λ_1 phase boundary has exponents $2-\alpha_s = 0$ and $2-\alpha_s' = 1.55(3)$ in Eq. (8). Since the model is symmetric in $\{c_1, c_2\}$, these results will be the same if instead the λ_2 phase boundary between the empty and c_2-dominated phases is crossed.

Scaling around the multicritical point: Scaling axes through the multicritical point are set up consistent with Fig. 7. The parallel scaling axis (parallel to the τ-phase boundary) runs along the τ phase boundary on the main diagonal from $(-5,-5)$ to (5,5). The transverse axis (transverse to the τ-line) runs along the λ_2 phase boundary and crosses the multicritical point into the c_1-dominated phase. Similarly, a second transverse axis runs along the λ_1 phase boundary into the c_2-dominated phase.

Estimates of the free energy f_L and its derivatives are plotted for $L = 20$ on the axes through the multicritical point in Fig. 13. The three top panels show results along the parallel scaling axis, while the bottom panels display results along the transverse scaling axis running along λ_2 and crossing into the c_1-dominated phase.

Since the phase diagram is symmetric about the main diagonal in the $\alpha\beta$ plane, and since the free energy is not a function of β in the c_1-dominated phase, and of α in the

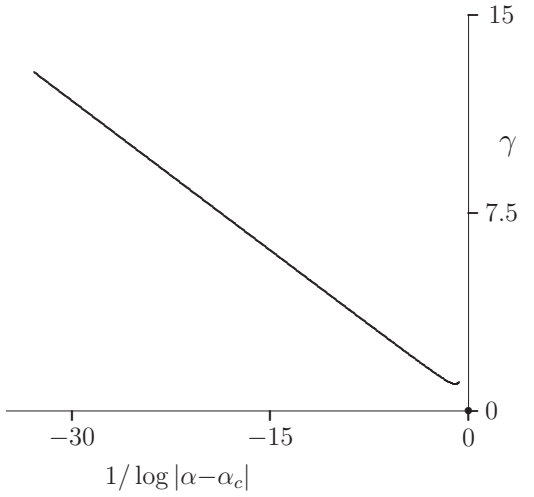

FIG. 12. Plotting $\gamma = \log(\langle c_1\rangle - \langle c_1\rangle|_{\mathrm{crit}})/\log|\alpha-\alpha_c|$ as a function of $1/\log|\alpha-\alpha_c|$ for the unlinked model along a line segment in the c_1-dominated phase starting in the λ_1 phase boundary with $\beta = -2$. In this graph $-0.9 \leqslant \alpha < 0$.

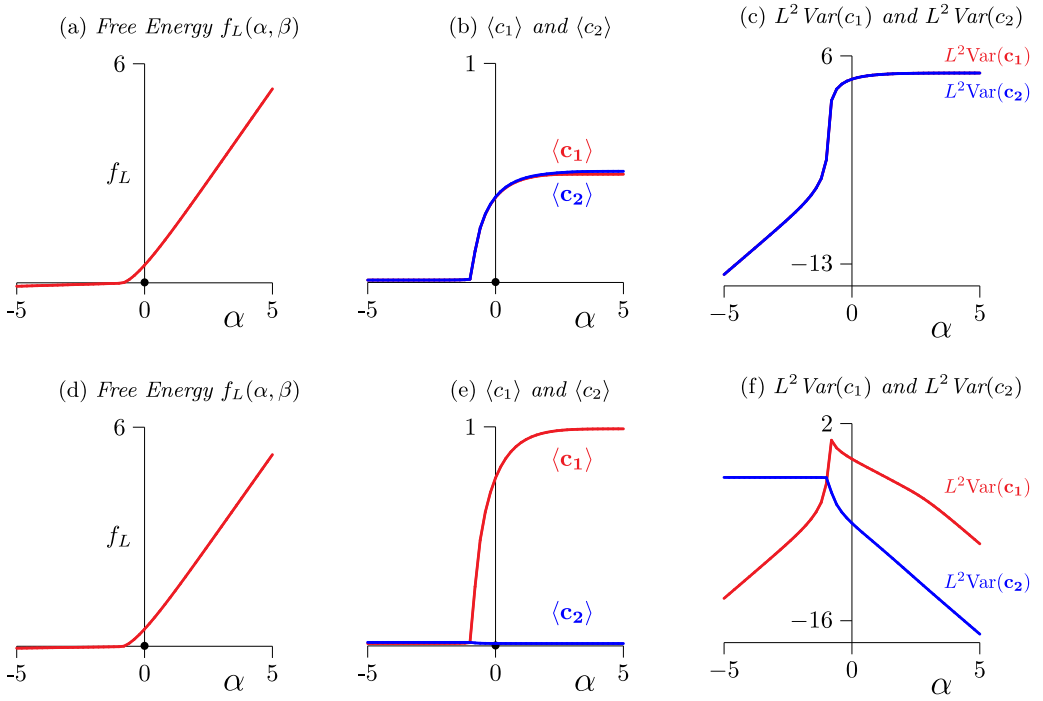

FIG. 13. Top panels: The free energy, mean concentrations, and variances of the unlinked model as a function of $\alpha = \beta$ along the line from the point $(-5, -5)$ to (5,5) through the multicritical point in the phase diagram in Fig. 9. The free energy (top left) shows a transition at approximately $\alpha_c = \beta_c \approx -\log \mu_2 \approx -0.97$ (as also seen in the graphs of the mean concentrations $\langle c_i\rangle$). These critical curves show a transition as the multicritical point is crossed into the dense phase where the polygons fill the confining square. The mean concentrations show a singular point in the free energy at the critical point, and the variances (plotted on a logarithmic scale) show a sharp increase at this point. Bottom panels: The free energy, mean concentrations, and variances as a function of α on the line through the multicritical point and with endpoints $(-5, \beta_c)$ and $(5, \beta_c)$ (where $\beta_c = -\log \mu_2 \approx -0.97$). These data show a continuous transition, similar to the transition seen in Fig. 8 between the empty phase, and the c_1-dominated phase.

c_2-dominated phase, it follows that the scaling of $\langle c_1\rangle$ and $\langle c_2\rangle$ along these axes is the same as that given in Eq. (20) with α_s' and α_s having the values in Eq. (23). This follows by symmetry, since $f_L(\alpha, \alpha_c) = f_L(\alpha, \beta)$ for any $\beta < \alpha_c$, and $f_L(\alpha, \alpha) = f_L(\alpha, \alpha_c)$ in the dense phases (that is, for $\alpha > \alpha_c$). Thus, it follows that the exponents α_u and α_t in Eqs. (9) and (10) have the same values as in Eq. (23), namely,

$$\alpha_u = \alpha_t \approx 0.45 \pm 0.03. \tag{24}$$

By Eq. (12), the crossover exponent in this model is $\phi = 1$. Taking into account the uncertainty of the estimate in Eq. (24), the estimate of the crossover exponent of the unlinked model is given by

$$\phi = 1.00 \pm 0.04. \tag{25}$$

B. The phase diagram of two linked confined square lattice polygons

In Fig. 14(a) a density plot of $g_L(\alpha, \beta)$ is shown (for $L = 20$) with the left bottom color low, and the right and top colors high. The free energy shows clear signs of phase transitions, and this is also seen in plots of the first and second derivatives of $g_L(\alpha, \beta)$, as shown in Figs. 14(b)–14(f).

The concentrations $\langle c_1\rangle$ and $\langle c_2\rangle$ [see Eq. (13)] are plotted in Figs. 14(b) and 14(c). These plots show a rapid change in the mean concentration of one, or both, $\langle c_1\rangle$ and $\langle c_2\rangle$ when phase boundaries are crossed. Note that these plots are different from those in Fig. 8, suggesting that the different topology of this model (namely, that the two polygons are linked in $\mathbb{R}^2$) has an impact on its thermodynamic properties.

The variances [Eq. (14)] and covariance [Eq. (15)] are plotted in Figs. 14(d)–14(f). The covariance shows (as expected) strong negative correlations between c_1 and c_2 induced by the confining square, except along two phase boundaries, where the correlation is positive. $\mathrm{Var}(c_1)$ in Fig. 14(e), considered with Fig. 14(b), shows a phase boundary τ_1 close to or on the main diagonal for $\alpha > \alpha_c$ and $\beta > \beta_c$, where (α_c, β_c) is the location of a multicritical point.

Magnifying Fig. 14(a) in the vicinity of the multicritical point gives the density plot in Fig. 15. This plot suggests that a *curved* phase boundary τ_2 separates the empty phase from a c_2-dominated phase for large positive β (in this phase the inner polygon is dense, and the outer polygon is expanded to near the perimeter of the confining square).

The rest of the phase diagram, as suggested by Figs. 14 and 15, is shown in Fig. 16. A vertical phase boundary runs along $\alpha = \alpha_c$ from the multicritical point for $\beta < \beta_c$. This phase boundary, denoted by λ, separates an empty phase, for large negative α and β, from a c_1-dominated phase for large positive α. This transition is similar to the transition across the λ_1 phase boundary in the unlinked model, and the critical value of α is given by $\alpha_c = -\log \mu_2$ (using an argument similar to the one used for λ_1 in the unlinked model). Crossing

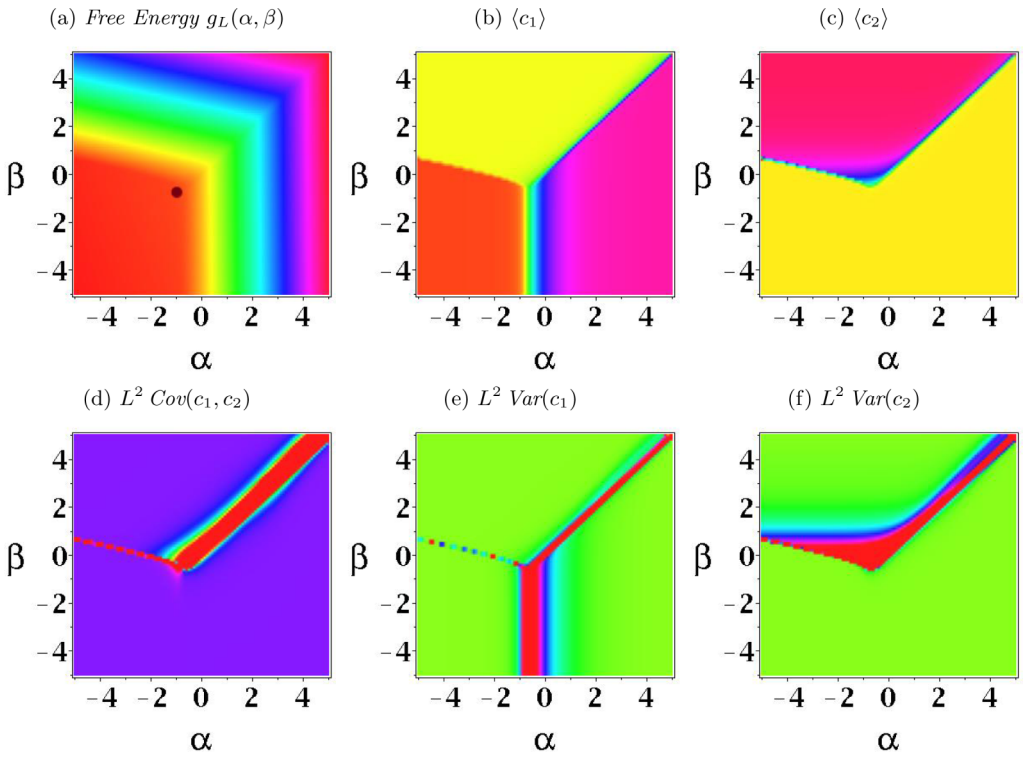

FIG. 14. The free energy $g_L(\alpha,\beta)$ of the linked model for $L = 20$ (top left), and its first and second derivatives. Proceeding clockwise from the top middle, the mean concentrations of the outer polygon $\langle c_1\rangle$ and the inner polygon $\langle c_2\rangle$, their variances $\mathrm{Var}(c_2)$ and $\mathrm{Var}(c_1)$, and the covariance of c_1 and c_2, $\mathrm{Cov}(c_1,c_2)$. The concentrations c_1 and c_2 are negatively correlated, and the covariance shows a sharp transition close to the main diagonal for $\alpha = \beta > \alpha_c$. In addition, a second, apparently weaker, phase transition appears along a curve starting in the multicritical point and running into the second quadrant, and a third phase transition runs vertically into the multicritical point from below. The approximate location of the multicritical point in the model is denoted by a bullet in panel (a).

λ takes the model from its empty phase into a phase where the outer polygon is dense, while the inner polygon remains small.

Since the multicritical point (α_c,β_c) is the intersection of the three phase boundaries λ, τ_1 and τ_2, with the λ phase boundary running vertically and separating the empty phase from the c_1-dominated phase, we conclude that $\alpha_c = -\log\mu_2 \approx -0.97$, but, as will be seen below, it appears from our numerical data that $\beta_c > -0.97$, although the resolution of our data was not good enough to confirm this.

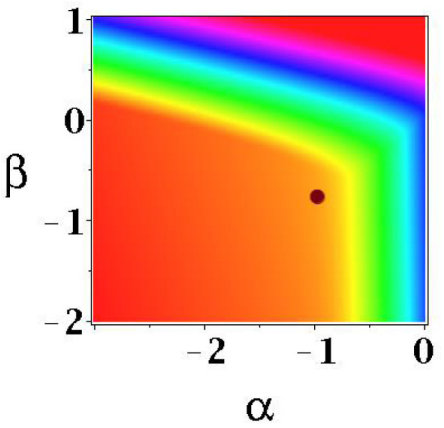

FIG. 15. A density plot the free energy $g_L(\alpha,\beta)$ of the linked model in the vicinity of the multicritical point. The location of the multicritical point is estimated to be $(\alpha,\beta) = (-0.97,-0.77)$ and is denoted by the bullet.

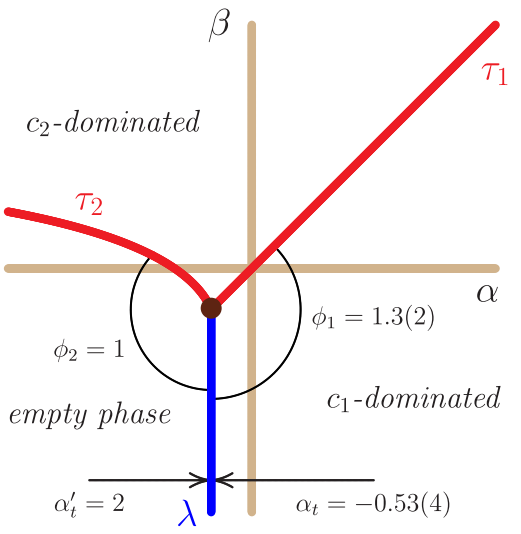

FIG. 16. Crossover exponents between the τ_1 and λ, and τ_2 and λ critical curves around the multicritical point in the phase diagram of the linked model.

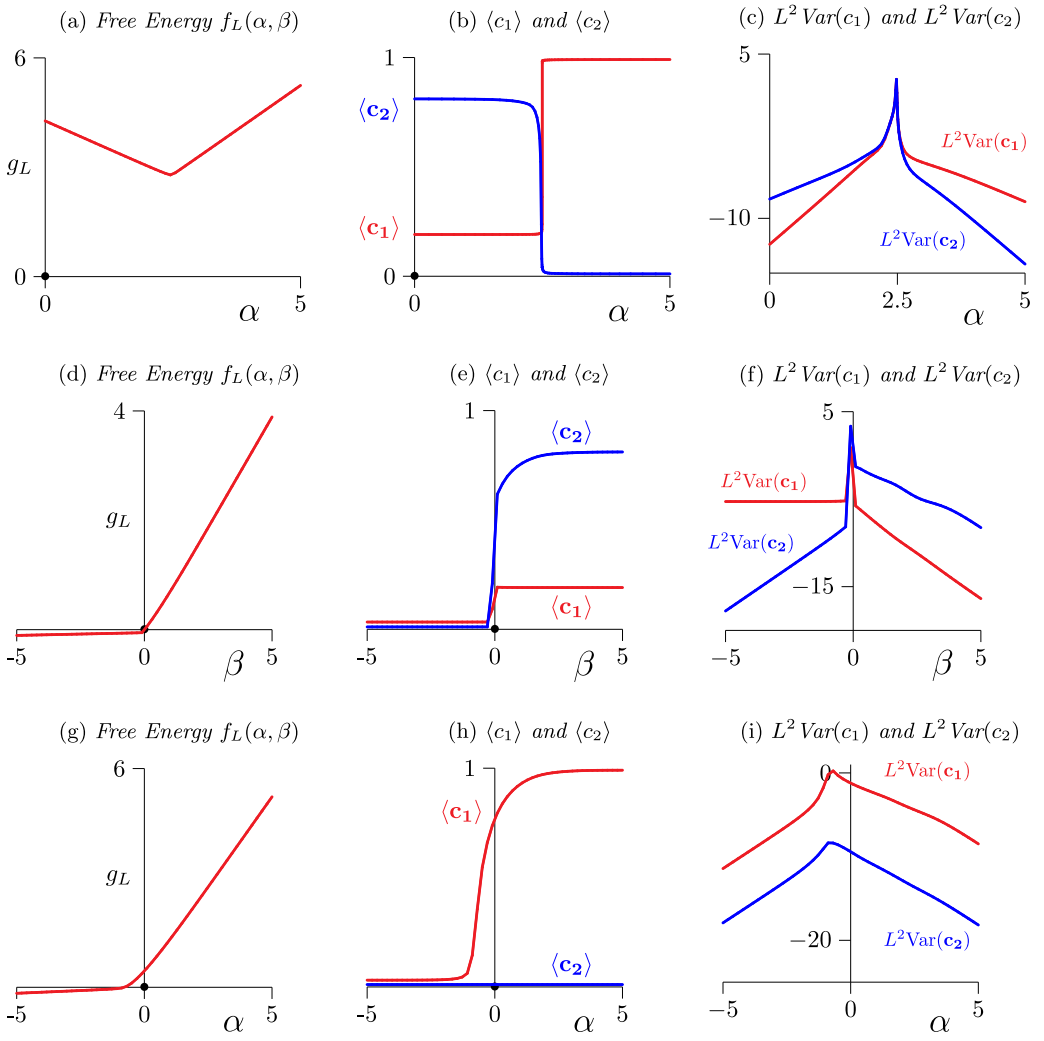

FIG. 17. Top row: The free energy, mean concentrations and variances of the linked model as a function of α along the line segment from (0,5) to (5,0) across the τ_1 phase boundary. The variances are plotted on a logarithmic vertical scale. Middle row: The free energy, mean concentrations and variances as a function of β on the line segment from the point $(-2,-5)$ to the point $(-2,5)$ across the τ_2 phase boundary. Bottom row: The free energy, mean concentrations and variances as a function of α on the line segment across the λ phase boundary from $(-5,-2)$ to $(5,-2)$.

The trajectories of τ_1 and τ_2 were estimated by fitting curves to points along the phase boundaries from our data sets. In the case of τ_1 a linear least squares fit using a quadratic model shows that

$$\tau_1(\alpha) \approx 0.0824 + 0.9824\,\alpha + 0.00268\,\alpha^2, \quad \text{for} \quad \alpha > -0.97. \tag{26}$$

Since along the critical curve λ the value of $\alpha = \alpha_c \approx -0.97$, it follows that this predicts that the multicritical point appears to be close to $(-0.97, -0.868)$.

In the case of τ_2 a 3-parameter nonlinear fit using the *NonlinearFit* function in the Statistics package of Maple17 [40] was used along points on the phase boundary. Assuming a powerlaw shape gives the trajectory

$$\tau_2(\alpha) \approx -0.6680 + 0.5184|-0.97 - \alpha|^{0.64}, \quad \text{for} \quad \alpha < -0.97. \tag{27}$$

This predicts that the multicritical point is close to $(-0.97, -0.668)$. Taking the average of this estimate, and the estimate obtained from the trajectory of the τ_1 phase boundary, gives our best estimate of the location of the multicritical point for the linked case:

$$(\alpha_c, \beta_c) \approx (-0.97, -0.77), \tag{28}$$

assuming, of course, that finite-size corrections at $L = 20$ are negligible. Note that the estimate of β_c is larger than the one reported for the unlinked model (namely, $\beta_c \approx -0.97$). This estimate may have a large confidence interval, since numerical estimates in the vicinity of the multicritical point are strongly affected by the environment (namely, it is the intersection of three phase boundaries).

Critical scaling in the linked model

The τ_1 phase boundary: In the top row of Fig. 17 the free energy and its derivatives are plotted as a function of α along

the line segment from (0,5) to (5,0) in the phase diagram. As in the unlinked model, the free energy can be fitted to an absolute value function using the model

$$w(\alpha, 5{-}\alpha) = a_0 + a_1\,\alpha + a_2\,|\alpha - \alpha_c|^{2-\alpha_s} + a_3\,(\alpha - \alpha_c)^2. \tag{29}$$

The curve in Fig. 17(a) appears to be rotated about its minimum, and to account for this, a linear term in α was included in Eq. (29). A fit with $a_3 = 0$ (so that there is no quadratic correction) gives

$$w(\alpha, 5{-}\alpha) \approx 2.3172 + 0.1823\,\alpha + 0.7747\,|\alpha - 2.4592|^{1.018}, \tag{30}$$

while including the quadratic term in the model gives

$$w(\alpha, 5{-}\alpha) \approx 2.3259 + 0.1819\,\alpha + 0.7737\,|\alpha - 2.4583|^{1.057} - 0.0124\,(\alpha - 2.4583)^2. \tag{31}$$

We note again the relative small coefficient of the quadratic term, suggesting minor curvature of the τ_1 phase boundary for $-0.97 \leqslant \alpha \leqslant 5$. Equation (27) shows that the τ_1 phase boundary is crossed approximately at the point (2.4592,2.5408) by the line segment from (0,5) to (5,0) in the phase diagram, consistent with the observation that the τ_1 phase boundary is slightly off-set from the main diagonal in the $\alpha\beta$ plane.

The critical exponents $2{-}\alpha_s$ and $2{-}\alpha'_s$ [see Eq. (8)] can also be read from the fits in Eqs. (30) and (31):

$$2 - \alpha_s = 2 - \alpha'_s = 1.02 \pm 0.04. \tag{32}$$

The error bar is the absolute difference between the estimates in Eqs. (30) and (31). These results are consistent with a first-order transition along τ_1 (which is seen in the jump discontinuities in $\langle c_1\rangle$ and $\langle c_2\rangle$ shown in the top middle graph in Fig. 17).

The τ_2 phase boundary: The free energy, concentrations and variances across this phase boundary are plotted in Fig. 17 along a line segment from $(-2, -5)$ to $(-2, 5)$. The jump discontinuities in $\langle c_1\rangle$ and $\langle c_2\rangle$ are consistent with this also being a first-order transition. Fits similar to Eqs. (30) and (31) give the approximations

$$w(-2, \beta) \approx -0.0392 + 0.4013\,\beta + 0.3517\,|\beta - 0.0517|^{1.059} \tag{33}$$

and

$$w(-2, \beta) \approx -0.0188 + 0.4017\,\beta + 0.3400\,|\beta - 0.0567|^{1.182} - 0.0151\,(\beta - 0.0567)^2. \tag{34}$$

Comparison of these fits with Eq. (8) give the estimated critical exponents

$$2 - \alpha_s = 2 - \alpha'_s = 1.06 \pm 0.12 \tag{35}$$

and critical point $(-2, \tau_2(-2)) \approx (-2, -0.52(5))$ on the τ_2 phase boundary. These values are again consistent with τ_2 being a curve of first-order transitions.

The λ phase boundary: The data along the λ phase boundary are plotted in the bottom panels of Fig. 17. The concentration $\langle c_1\rangle$ plotted in Fig. 17(h) is obtained from estimates along the line segment between the points $(-5, -2)$ and $(5, -2)$ in the phase diagram. In this graph $\langle c_1\rangle$ has a profile consistent with a continuous transition.

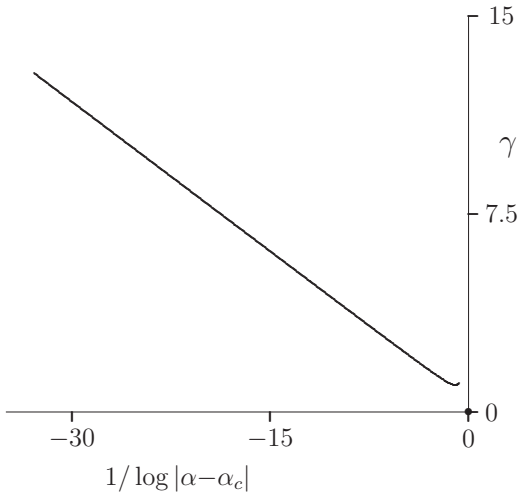

FIG. 18. Plotting $\gamma = \log(\langle c_1\rangle - \langle c_1\rangle|_{\rm crit})/\log|\alpha{-}\alpha_c|$ as a function of $1/\log|\alpha{-}\alpha_c|$ for the linked model in the c_1-dominated phase along a line segment starting in the λ phase boundary, with $\beta = -2$. In this graph $-0.9 \leqslant \alpha \leqslant 0$.

As in the unlinked model, the scaling exponent α'_s in Eq. (8) can be estimated by plotting $\log\langle c_1\rangle_s/\log|\alpha{-}\alpha_c|$ [Eq. (22)] as a function of $1/\log|\alpha{-}\alpha_c|$. Plotting γ in Eq. (22) as a function of $1/\log|\alpha{-}\alpha_c|$ for $-0.95 \leqslant \alpha \leqslant 0$ gives the graph in Fig. 18. Fitting a linear function in $1/\log|\alpha{-}\alpha_c|$ to the graph gives the estimate $1{-}\alpha'_s \approx 0.57$, and fitting a quadratic instead gives $1{-}\alpha'_s \approx 0.63$. The difference in these two estimates is taken as a confidence interval in the estimate.

On the empty phase side of λ the free energy is constant to numerical accuracy, and so one expects $\alpha_s = 2$. Taken together,

$$\alpha_s = 2 \quad \text{and} \quad \alpha'_s \approx 0.43 \pm 0.06. \tag{36}$$

This shows that $2{-}\alpha_s = 0$ on the empty phase side of λ, and $2{-}\alpha'_s = 1.57(6)$ on the c_1-dominated phase side.

Scaling around the multicritical point: In the phase diagram in Fig. 16 a transverse scaling axis is set up to run horizontally through the multicritical point, while two parallel scaling axes are set up to run along the first phase order phase boundaries.

The free energies, mean concentrations and variances of the concentrations are plotted along the parallel and transverse scaling axes in Fig. 19. Along the transverse axis [shown in Fig. 19(h)] our data show that the concentrations remain unchanged when compared to Fig. 17(h). Thus, the transverse scaling exponents are the same as those found along the λ phase boundary given in Eq. (35), namely, $\alpha_t = 2$ from the τ_2 side of the phase boundary, and $\alpha_t = 0.43(6)$ on the τ_1 side.

Since the trajectory of the τ_1 phase boundary and location of the multicritical point are not known exactly, it is more challenging to estimate the scaling exponent α_u. Putting $\ell(\alpha) = [\alpha, \tau_1(\alpha)]$ and denoting the distance along τ_1 between $\ell(\alpha_c)$ and $\ell(\alpha)$ in the $\alpha\beta$ plane by $d(\alpha_c, \alpha)$, the exponent α_u can be estimated by calculating the ratio $\log\langle c_1\rangle_s/\log d(\alpha_c, \alpha)$ with $\alpha_c = -0.970$ along τ_1 [see Eqs. (21) and (22)]. By the

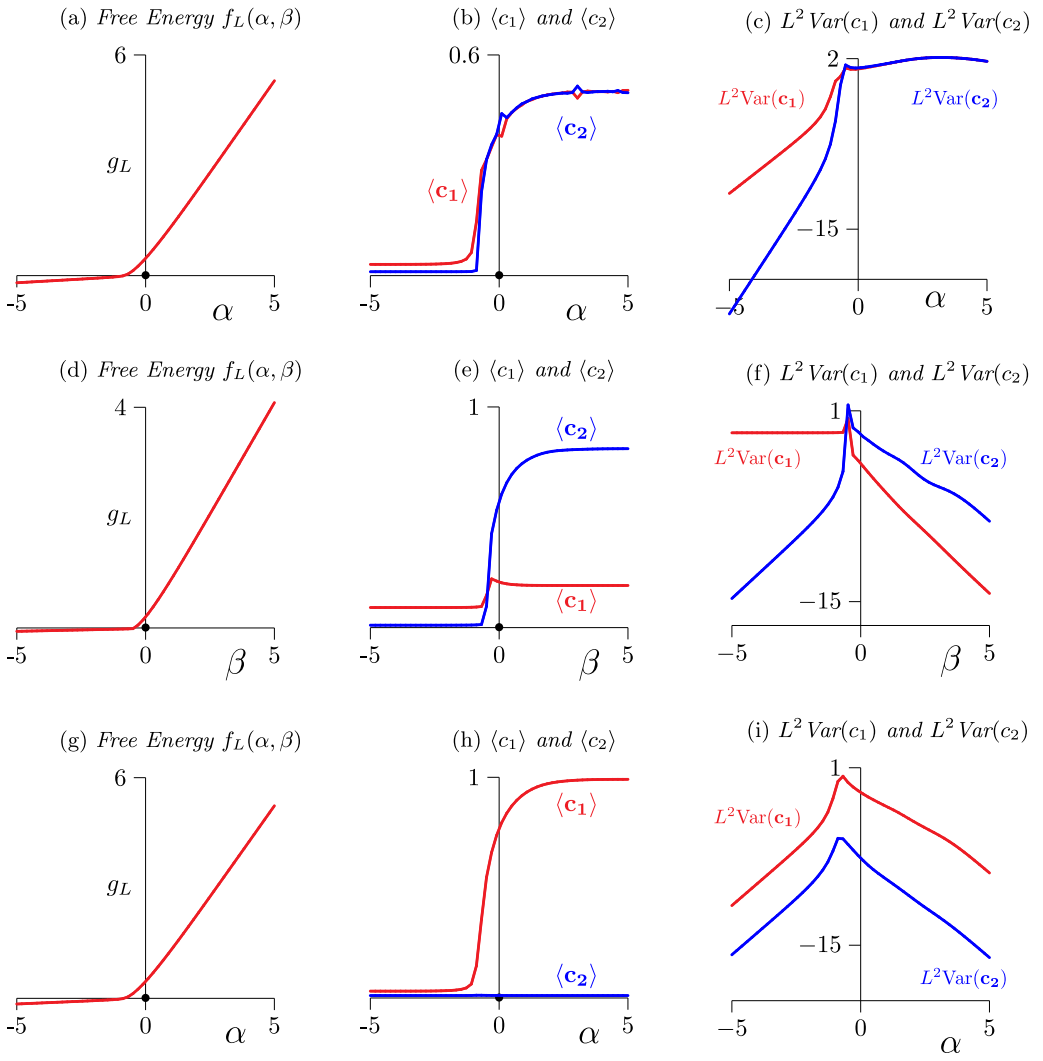

FIG. 19. Top row: The free energy, mean concentrations and variances of the linked model as a function of α from the empty phase and then along the τ_1 phase boundary. The variances are plotted on a logarithmic vertical scale. Middle row: The free energy, mean concentrations and variances as a function of β along the λ phase boundary and tangent to the τ_2 phase boundary at the multicritical point. The data is plotted against β along the line segment from $(\alpha_c, -5)$ to the point $(\alpha_c, 5)$. Bottom row: The free energy, mean concentrations and variances as a function of α transverse to the λ phase boundary thought the multicritical point along the line segment from $(-5, \beta_c)$ to $(5, \beta_c)$ into the c_1-dominated phase.

same arguments leading to Eq. (22), we plot

$$\gamma = \log\langle c_1\rangle_s / \log d(\alpha_c, \alpha) \tag{37}$$

as a function of $1/\log d(\alpha_c, \alpha)$ and estimate the exponent $1-\alpha_u$ by a linear fit. This gives the graph in Fig. 20.

A linear fit to the data in Fig. 20 gives $1-\alpha_u \approx 0.172$ and a quadratic fit gives $1-\alpha_u \approx 0.242$. Taking the difference as an error bar gives the estimate $1-\alpha_u = 0.17 \pm 0.07$. Thus, our estimate is

$$\alpha_u = 0.83 \pm 0.07, \quad \text{along } \tau_1. \tag{38}$$

Comparing this with the estimate of α_t on the c_1-dominated phase side of the λ gives the estimated crossover exponent $\phi_1 = 1.3 \pm 0.2$, by Eq. (12).

Along the τ_2 phase boundary the situation is simpler. This phase boundary is between the empty phase and the c_2-dominated phase, and the free energy is continuous along τ_2. Since the free energy in the scaling limit is a constant in the empty phase, it is also, by continuity, a constant along the τ_2 phase boundary in the scaling limit. Thus, one concludes that $\alpha_u = 2$ along τ_2, whereas the transverse exponent on the empty phase side of λ is $\alpha_t = 2$ as well. This gives the crossover exponent $\phi = 1$ between the λ and τ_2 phase boundaries.

C. Finite-size effects

In the previous sections we have considered the phase diagrams for $L = 20$. In this section we briefly consider finite-size effects in our data. We do this only for the linked model; finite-size effects in the unlinked model are smaller and phase boundaries do not move with increasing L.

In Fig. 21(a) the concentrations $\langle c_1\rangle$ are plotted along a line segment as the λ phase boundary is crossed into the c_1-dominated phase in the linked model, for models of sizes $L = 8$, 12, 16, and 20. The graphs show rapid convergence

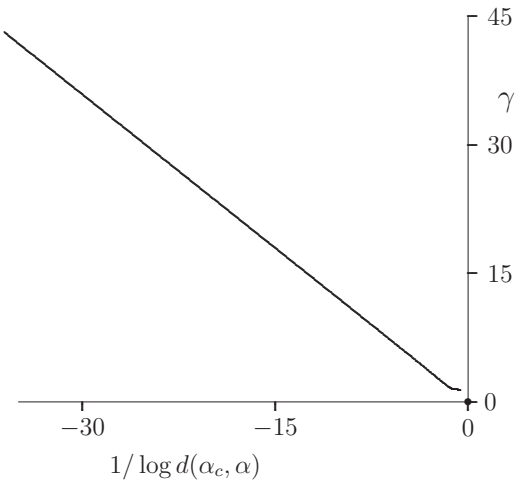

FIG. 20. Plotting $\gamma = \log(\langle c_1\rangle - \langle c_1\rangle|_{\rm crit})/\log d(\alpha_c,\alpha)$ as a function of $1/\log d(\alpha_c,\alpha)$ for the linked model along the trajectory of the τ_1 phase boundary, starting in the multicritical point. In this graph $-0.9 \leqslant \alpha \leqslant -0.2$.

toward a limiting curve with increasing L, particularly in the c_1-dominated phase. Finite-size effects are most pronounced close to the critical point, and is seen in the slight upturn of the plot in Fig. 18 when α approaches α_c. We accommodated for this by fitting a linear function to data, while discarding data close to the critical point.

Figure 21(b) is a graph of the variance $\mathrm{Var}(c_1)$ plotted along a line segment from (0,5) to (5,0) crossing the τ_1 phase boundary, for $L = 8$, 12, 16, and 20. These curves all spike sharply when τ_1 is crossed when $\alpha \approx 2.48$. The heights of the spikes increase by almost doubling as L increments by 4. Finite-size effects can be seen in the slight broadening at the base of the spikes, and this broadening decreases with increasing L.

The variance $\mathrm{Var}(c_2)$ plotted along a vertical line from $(-2,-2)$ to $(-2,3)$ across the τ_2 phase boundary is shown in Fig. 21(c) for $L = 8$, 12, 16, and 20. For each L this shows a spike roughly twice the height of the spikes in Fig. 21(b). With increasing L the spikes move, towards the left, but with decreasing increments. This shows that the location of the τ_2 phase boundary remains uncertain, but also that it should converge to a limiting curve of first-order transitions along which $\mathrm{Var}(c_2)$ is divergent.

IV. CHARACTERIZING THE TRANSITIONS

The nature of transitions across phase boundaries in these models can also be explored by defining and tracking order parameters and metric observables as the system is taken through a transition. Numerical estimates of order parameters were obtained by sampling the models using a multiple Markov chain metropolis algorithm [28,41,42] implementing BFACF elementary moves (see Fig. 3) [26,27] on each polygon. In our particular implementation we sampled along 50 Markov chains (performing 10^5 iterations along each sequence) along lines in the $\alpha\beta$ plane. Apart from tracking the lengths n_1 and n_2 of the polygons, these simulations also collected data on the number of nearest neighbor contacts k_1 and k_2 in each polygon (these are *self-contacts*), as well as the number of nearest neighbor contacts k_m between polygons (these are *mutual contacts*).

Let $w_L(n_1,n_2;k_1,k_2,k_m)$ be the number of conformations of the unlinked or linked model in a square of side-length L, of lengths n_1 and n_2, respectively, with k_1 self-contacts in the first polygon, k_2 in the second, and k_m mutual contacts. The mean *density of self-contacts* of the first polygon is defined by

$$\langle k_1/L^2\rangle = \frac{\sum_{k_1,k_2,k_M}^{n_1,n_2} (k_1/L^2)\, u_L(n_1,n_2;k_1,k_2,k_M)\, e^{\alpha n_1}\, e^{\beta n_2}}{\sum_{k_1,k_2,k_M}^{n_1,n_2} u_L(n_1,n_2;k_1,k_2,k_M)\, e^{\alpha n_1}\, e^{\beta n_2}}. \tag{39}$$

The densities $\langle k_2/L^2\rangle$ of self-contacts in the second polygon, and $\langle k_m/L^2\rangle$ of mutual contacts, are defined similarly.

We sampled data on metric observables, namely, the mean-square radius of gyration of the first polygon [a function of (α,β)], $\langle r_1^2\rangle$, and the corresponding quantity for the second polygon, $\langle r_2^2\rangle$. Moreover, we look at the mean distance or separation between the centers-of-mass of the two polygons, $\langle d_{\rm cm}\rangle$.

In addition to these quantities, the correlations $\mathrm{Cor}(k_1,k_2) = \langle k_1k_2\rangle - \langle k_1\rangle\langle k_2\rangle$ (between self-contacts in

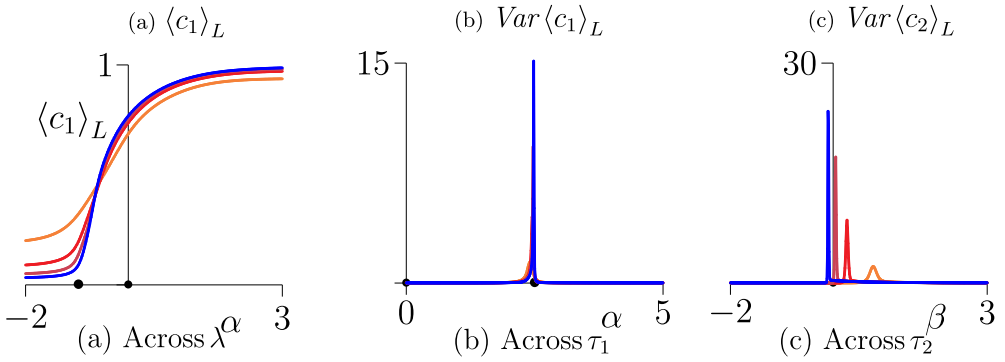

FIG. 21. (a) The concentration of the outer polygon in the linked model along a line segment with $\beta = -2$ crossing the λ phase boundary in the c_1-dominated phase, for system sizes $L = 8$, 12, 16, and 20. The location of the critical point is denoted by a bullet (b).

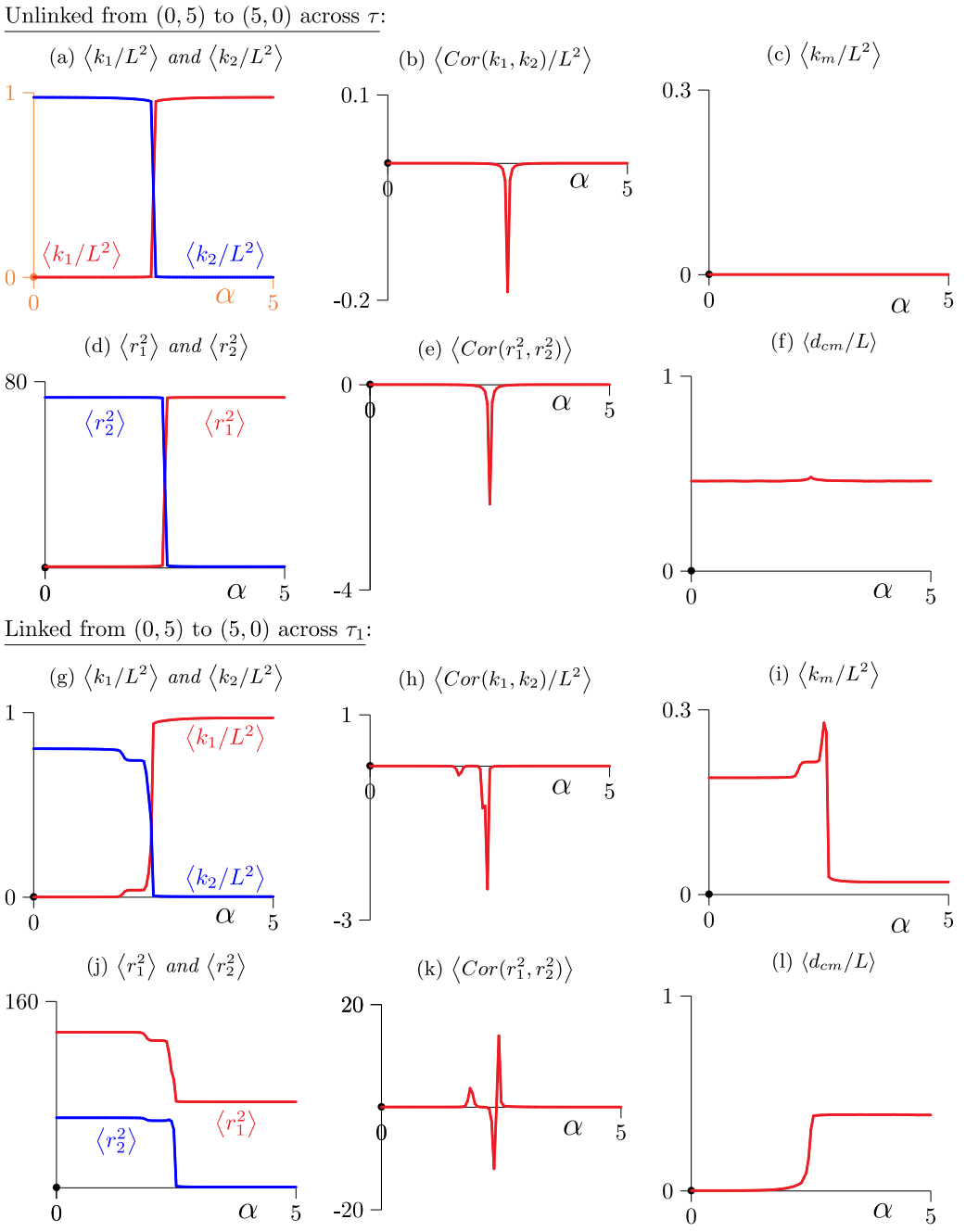

FIG. 22. Across the τ and τ_1 phase boundaries in the $\alpha\beta$ plane. Graphs for the unlinked model are shown in panels (a–f) and for the linked model are shown in panels (g–l). Consistent with the results in Figs. 10(a)–10(c) and 17(a)–17(c), these results show first-order transitions as the τ and τ_1 phase boundaries are crossed in the two models, respectively.

the polygons), and $\mathrm{Cor}(r_1^2, r_2^2) = \langle r_1^2\, r_2^2\rangle - \langle r_1^2\rangle\langle r_2^2\rangle$ (between the square radii of gyration of the two polygons) were calculated.

In Fig. 22 we show thermodynamic and metric data estimates along the line segment with endpoints (0,5) and (5,0) in the phase diagram for the unlinked model (Fig. 10) and the linked model (Fig. 17). This line crosses the τ phase boundary in the unlinked model, and the τ_1 phase boundary in the linked model. The results for the unlinked model are shown in Figs. 22(a)–22(f), while the results for the linked model are shown in Figs. 22(g)–22(l).

The results in both models are consistent with a first-order transition as the phase boundaries (τ or τ_1, respectively) are crossed. There are sharp discontinuities in the mean number of self-contacts in both models, as well as in the metric quantities. The correlations show sharp peaks at the critical points. Figure 22(j) indicates that the outer polygon in the linked model is inflated by the inner polygon in the c_2-dominated phase, and expands in the c_1-dominated phase to compress the inner polygon to a very small size.

In Fig. 23 the estimated mean quantities are plotted as the linked model is taken through the τ_2 phase boundary. The

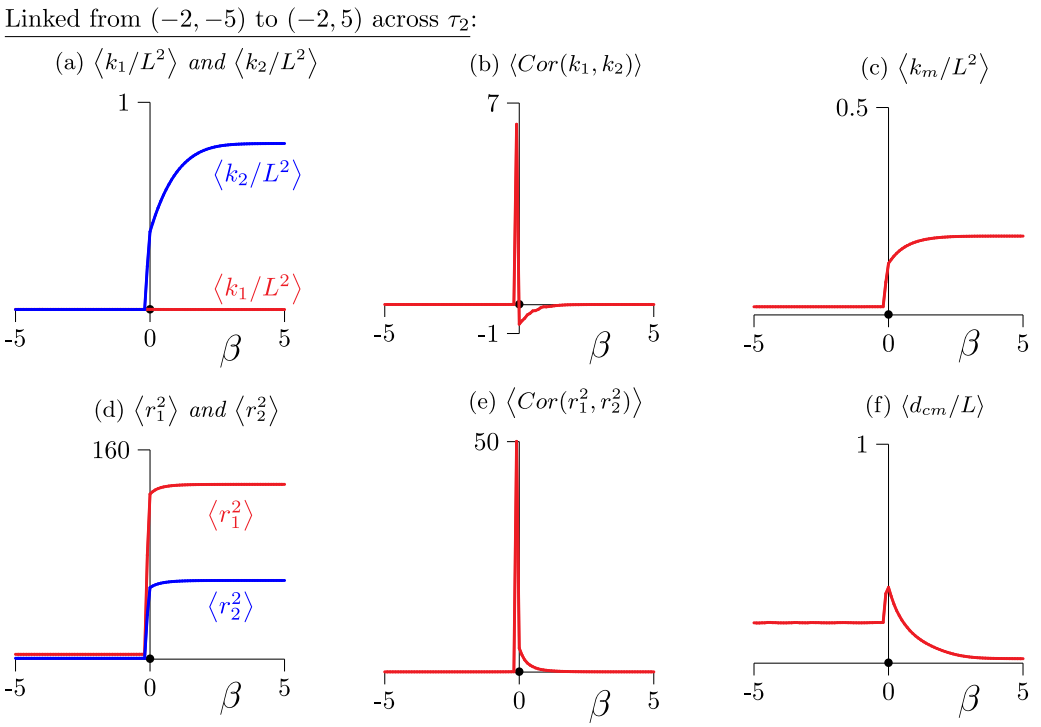

FIG. 23. Across the τ_2 phase boundary in the $\alpha\beta$ plane (linked model). Consistent with the results in Figs. 17(d)–17(f), these results show a first-order phase transition with sharp peaks in the correlation functions as the phase is crossed.

results are consistent with those in Figs. 17(d)–17(f), showing a strong first-order character as the inner polygon inflates the outer polygon when the model is taken from the empty phase into the c_2-dominated phase in Fig. 16. The mean number of self-contacts in the inner polygon changes discontinuously at the phase boundary, as the mean-square radii of gyration of both polygons change discontinuously.

In Fig. 24 we show changes in order parameters as the λ_1 (or λ_2) phase boundary is crossed in the unlinked model, and the similar changes as the λ boundary is crossed in the linked model. Our results in the previous sections show that these are continuous phase boundaries, and the results in Fig. 24 are consistent with this. The mean density of self-crossings in Fig. 24(a) (across the λ_1 phase boundary), and Fig. 24(g) (across the λ phase boundary) show very similar behavior in the two models. Crossing these boundaries into the c_1-dominated phase causes the first polygon in the unlinked model, and the outside polygon in the linked model, to expand into the dense phase occupying almost all sites in the confining square. The second polygon (in the unlinked model) and the inside polygon (in the linked model) are in both cases squeezed to minimal length by the expanding polygon, and this is consistent with the metric data reported in the figure. The mean distance between the centers-of-mass in the unlinked model decreases from the mean distance in the empty phase to a smaller distance as one polygon increases in length, while in the linked model, the distance in the empty phase is zero, but becomes positive when the outer polygon expands into the c_1-dominated phase with center-of-mass near the center of the confining square, while the inner polygon has almost minimal length and explores the inside of the square. These observations are in contrast with the results seen in Fig. 23, where a first-order transition is seen along the τ_2 phase boundary in the linked model.

V. CONCLUSIONS

We determined the phase diagrams of two square lattice models of pairs of ring polymers in the dense phase. The placements of the two polygons in a confining square were chosen in two distinct topological ways, in one case they were unlinked (or splittable) in the plane, and in the second case, linked (or unsplittable) in the plane. The phase diagrams include, in addition to an empty phase, a phase dominated by the first polygon (it is dense inside the square), and a phase dominated by the second polygon, and are shown in Figs. 9 and 16. These phases are separated by critical curves whose nature depends on the topology of the model. In the unlinked model, there are two lines of continuous transitions (λ_1 and λ_2) separating the empty phase from the two dense phases, while the two dense phases are separated by a line of first-order transitions (τ). In contrast, the linked model has two curves of first-order transitions (τ_1 and τ_2), where τ_1 separates a phase in which the outer polygon is dense from a phase in which the inner polygon is dense, and τ_2 separates the empty phase from the dense inner polygon phase. A line of continuous transitions λ separates the empty phase from the dense outer polygon phase.

In the case of both models we were able to determine critical exponents along the critical curves. Along the curves of first-order transition the exponents are given in Eqs. (19) (for τ), (32) (τ_1), and (35) (τ_2). In each case the result is consistent with the expected value $2-\alpha_s = 2-\alpha'_s = 1$ reported in Eq. (5). We were similarly able to estimate these exponents

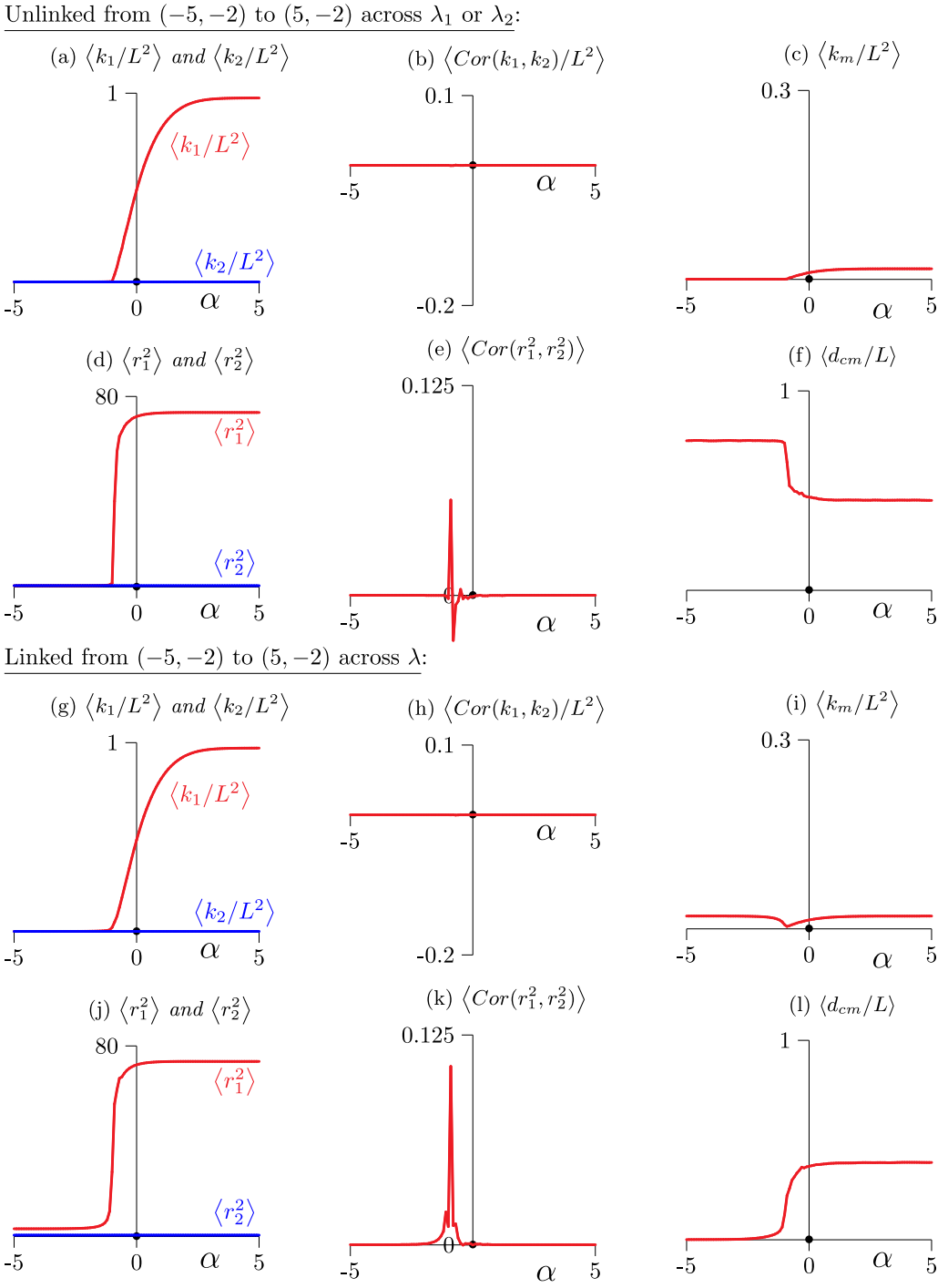

FIG. 24. Across the λ_1 (or λ_2) and λ phase boundaries in the $\alpha\beta$ plane. Graphs for the unlinked model are shown in (a–f), and for the linked model are shown in (g–l). Consistent with the results in Figs. 8(a)–8(c) and 19(g)–19(i), these results show continuous transitions as these phase boundaries are crossed in the two models, respectively.

along the lines of continuous transitions. The results are shown in Table I.

The concentration gap associated with the first-order transitions may also be estimated. For example, for the critical line τ in the unlinked model the free energy crossing τ is given by Eq. (17). Taking derivatives on either side of τ and subtracting to determine the gap gives $H_\tau \mid_{\alpha=2.5} \approx 1.95$. In the same way, by Eqs. (27) and (29), $H_{\tau_1} \mid_{\alpha=2.5} \approx 1.55$ and $H_{\tau_2} \mid_{\alpha=-2.0} \approx 0.70$.

TABLE I. Estimates of $2-\alpha_s$ and $2-\alpha_s'$ across phase boundaries.

	Unlinked model			Linked model		
	τ	λ_1	λ_2	τ_1	τ_2	λ
$2-\alpha_s$	1.003(3)	0	0	1.02(4)	1.06(12)	0
$2-\alpha_s'$	1.003(3)	1.55(3)	1.55(3)	1.02(4)	1.06(12)	1.57(6)

TABLE II. Estimates of $2-\alpha_t$ and $2-\alpha_u$ between τ and λ boundaries.

	Unlinked model		Linked model	
	τ-λ_1	τ-λ_2	τ_1-λ	τ_2-λ
$2-\alpha_t$	1.55(3)	1.55(3)	1.57(6)	0
$2-\alpha_u$	1.55(3)	1.55(3)	1.17(7)	0
ϕ	1.00(4)	1.00(4)	1.3(2)	1

Multicritical scaling around the multicritical points was more difficult to determine, in particular in the linked model. Our estimates of the critical exponents are less secure in the linked model. We show our best estimates in Table II.

Finally, we note that exact enumeration methods may be used to determine the partition functions in Eqs. (1) and (2) for squares of side-length $L = 20$. The methods in Refs. [43,44] seem particularly suited for a study like this. In the cubic lattice such exact enumeration methods will be less effective, and approximate enumeration methods, including the GAS and GARM algorithms, will perform better. For example, in Ref. [18] the GAS algorithm was used to approximately enumerate knotted polygons in a confining cube of dimensions 15^3.

ACKNOWLEDGMENTS

E.J.J.v.R. acknowledges financial support from NSERC (Canada) in the form of Discovery Grant No. RGPIN-2019-06303. E.J.J.v.R. is also grateful to the Department of Physics and Astronomy at the University of Padova for the financial support.

[1] M. Delbrück, Knotting problems in biology, Proc. Symp. Appl. Math. **14**, 55 (1962).
[2] P.-G. de Gennes, Tight knots, Macromol **17**, 703 (1984).
[3] K. Koniaris and M. Muthukumar, Knottedness in Ring Polymers, Phys. Rev. Lett. **66**, 2211 (1991).
[4] M. Baiesi and E. Orlandini, Universal properties of knotted polymer rings, Phys. Rev. E **86**, 031805 (2012).
[5] V. V. Rybenkov, N. R. Cozzarelli, and A. V. Vologodskii, Probability of DNA knotting and the effective diameter of the DNA double helix, Proc. Nat. Acad. Sci. U.S.A. **90**, 5307 (1993).
[6] S. Y. Shaw and J. C. Wang, Knotting of a DNA chain during ring closure, Science **260**, 533 (1993).
[7] A. Y. Grosberg, A. Feigel, and Y. Rabin, Flory-type theory of a knotted ring polymer, Phys. Rev. E **54**, 6618 (1996).
[8] J. P. J. Michels and F. W. Wiegel, Probability of knots in a polymer ring, Phys. Lett. A **90**, 381 (1982).
[9] E. J. Janse van Rensburg and S. G. Whittington, The BFACF algorithm and knotted polygons, J. Phys. A: Math. Gen. **24**, 5553 (1991).
[10] E. J. Janse van Rensburg, The probability of knotting in lattice polygons, Contemp Math. **304**, 125 (2002).
[11] R. Matthews, A. A. Louis, and J. M. Yeomans, Confinement of knotted polymers in a slit, Mol. Phys. **109**, 1289 (2011).
[12] C. Vanderzande, On knots in a model for the adsorption of ring polymers, J. Phys. A: Math. Gen. **28**, 3681 (1995).
[13] M. C. Tesi, E. J. Janse van Rensburg, E. Orlandini, D. W. Sumners, and S. G. Whittington, Knotting and supercoiling in circular DNA: A model incorporating the effect of added salt, Phys. Rev. E **49**, 868 (1994).
[14] E. Orlandini, A. L. Stella, and C. Vanderzande, Loose, flat knots in collapsed polymers, J. Stat. Phys. **115**, 681 (2004).
[15] E. J. Janse van Rensburg, E. Orlandini, M. C. Tesi, and S. G. Whittington, Knotting in stretched polygons, J. Phys. A: Math. Theo. **41**, 015003 (2008).
[16] E. J. Janse van Rensburg, E. Orlandini, M. C. Tesi, and S. G. Whittington, Knot probability of polygons subjected to a force: a Monte Carlo study, J. Phys. A: Math. Theo. **41**, 025003 (2008).
[17] E. J. Janse van Rensburg, Squeezing knots, J. Stat. Mech.: Theo. Expr. (2007) P03001.
[18] E. J. Janse van Rensburg, Osmotic pressure of compressed lattice knots, Phys. Rev. E **100**, 012501 (2019).
[19] F. Gassoumov and E. J. Janse van Rensburg, Osmotic pressure of confined square lattice self-avoiding walks, J. Phys. A: Math. Theor. **52**, 025004 (2018).
[20] P.-G. de Gennes, *Scaling Concepts in Polymer Physics* (Cornell, Ithaca, NY, 1979).
[21] A. Milchev, V. Yamakov, and K. Binder, Escape transition of a polymer chain: Phenomenological theory and Monte Carlo simulations, Phys. Chem. Chem. Phys. **1**, 2083 (1999).
[22] P. Cifra and T. Bleha, Piston compression of semiflexible ring polymers in channels, Macromol Theo. Sim. **30**, 2100027 (2021).
[23] J. M. Hammersley, The number of polygons on a lattice, Proc. Camb. Phil. Soc. **57**, 516 (1961).
[24] J. M. Hammersley and K. W. Morton, Poor man's Monte Carlo, J. Roy. Stat. Soc. Ser. B (Meth) **16**, 23 (1954).
[25] J. M. Hammersley and D. J. A. Welsh, Further results on the rate of convergence to the connective constant of the hypercubical lattice, Quart J. Math. **13**, 108 (1962).
[26] B. Berg and D. Foerster, Random paths and random surfaces on a digital computer, Phys. Lett. B **106**, 323 (1981).
[27] C. Aragao de Carvalho, S. Caracciolo, and J. Fröhlich, Polymers and $g\phi^4$-theory in four dimensions, Nucl. Phys. B **215**, 209 (1983).
[28] M. C. Tesi, E. J. Janse van Rensburg, E. Orlandini, and S. G. Whittington, Monte Carlo study of the interacting self-avoiding walk model in three dimensions, J. Stat. Phys. **82**, 155 (1996).
[29] S. Campbell and E. J. Janse van Rensburg, Parallel PERM, J. Phys. A: Math. Theo. **53**, 265005 (2020).
[30] E. J. Janse van Rensburg and A. Rechnitzer, Generalized atmospheric sampling of knotted polygons, J. Knot Theo. Ram **20**, 1145 (2011).
[31] A. Rechnitzer and E. J. Janse van Rensburg, Generalized atmospheric Rosenbluth methods (GARM), J. Phys. A: Math. Theo. **41**, 442002 (2008).

[32] M. N. Rosenbluth and A. W. Rosenbluth, Monte Carlo calculation of the average extension of molecular chains, J. Chem. Phys. **23**, 356 (1955).

[33] H.-P. Hsu and P. Grassberger, A review of Monte Carlo simulations of polymers with perm, J. Stat. Phys. **144**, 597 (2011).

[34] T. Prellberg and J. Krawczyk, Flat Histogram Version of the Pruned and Enriched Rosenbluth Method, Phys. Rev. Lett. **92**, 120602 (2004).

[35] M. Bousquet-Mélou, A. J. Guttmann, and I. Jensen, Self-avoiding walks crossing a square, J. Phys. A: Math. Gen. **38**, 9159 (2005).

[36] I. G. Enting and I. Jensen, Exact enumerations, In *Polygons, Polyominoes and Polycubes*, Vol. 775 of Lecture Notes in Physics, edited by A. J. Guttman (Springer, Berlin, 2009), pp. 143–147.

[37] N. Madras, Critical behavior of self-avoiding walks that cross a square, J. Phys. A: Math. Gen. **28**, 1535 (1995).

[38] E. J. Janse van Rensburg, Composite models of polygons, J. Phys. A: Math. Gen. **32**, 4351 (1999).

[39] I. D. Lawrie and S. Sarlbach, Tricriticality, in *Phase Transitions and Critical Phenomena*, Vol. 9, edited by C. Domb and J. L. Lebowitz (Academic Press, San Diego, CA, 1984).

[40] Maple 17, Waterloo Maple, Inc.

[41] N. Metropolis, A. W. Rosenbluth, M. N. Rosenbluth, A. H. Teller, and E. Teller, Equation of state calculations by fast computing machines, J. Chem. Phys. **21**, 1087 (1953).

[42] C. J. Geyer and E. A. Thompson, Annealing Markov chain Monte Carlo with applications to ancestral inference, J. Amer. Stat. Assoc. **90**, 909 (1995).

[43] H. Iwashita, Y. Nakazawa, J. Kawahara, T. Uno, and S. Minato, Efficient computation of the number of paths in a grid graph with minimal hash functions, Tech. Rep. Hokkaido University, Div. Comp. Sci., Ser. A, TCS-TR-A-13-64, 2013.

[44] S. Minato, Power of enumeration—Recent topics on BDD/ZDD-based techniques for discrete structure manipulation, in *IEICE Transactions on Information and Systems*, E100-D(8) (IEICE, Tokyo, 2017), pp. 1556–1562.